Proceedings of the ECCOMAS Thematic International Conference on Simulation and Modeling of Biological Flows (SIMBIO 2011)
September 21–23, 2011, VUB, Brussels, Belgium

Time–resolved measurements of wall-shear stress, dilatation, and static pressure in an elastic, stenotic vessel

Kai Pielhop, Kato Kentaro, Michael Klaas, and Wolfgang Schröder

Institute of Aerodynamics and Chair of Fluid Mechanics, RWTH Aachen University
Wüllnerstr. 5a, 52062, Aachen, Germany, k.pielhop@aia.rwth-aachen.de

Abstract

Stenosis significantly alters the flow field inside a blood vessel not only through geometric changes but also due to changing the mechanical properties of the vessel. To gain a better understanding of the fluid-structure interaction and the influence of these changes on the flow field, time-resolved measurements of the velocity field, the static pressure, and the vessel wall movement have to be performed synchronously. In this study, time-resolved particle-image velocimetry (TRPIV) is combined with simultaneous measurements of the static pressure inside an elastic, axisymmetric stenosed, transparent vessel at pulsatile flow. Peak Reynolds numbers Re_D from 310 to 690 combined with Womersley numbers Wo from 7.5 to 13 are investigated. A wall detection algorithm is applied to the TRPIV-data to determine the respective vessel wall position and the mechanical response of the elastic vessel on the flow conditions. The detected wall position is used to eliminate the wall curvature via a transformation algorithm and to enhance the wall-shear stress estimate. The TRPIV measurements show the stenosis to strongly change the flow conditions and induce complex flow structures like ring vortices. The footprints of these ring vortices are clearly identified in the unsteady wall-shear stress distribution. A phase analysis shows the coherence of local dilatation and static pressure at the respective position. The local dilatation evidences the load applied to the vessel model to depend on the axial position. A comparison of the theoretical static pressure difference with the measured static pressure difference evidences the frequency response of the elastic system to have a significant influence on the flow field in the investigated frequency range. That is at frequencies below the eigenfrequency a jet-like flow pattern develops in the downstream direction, whereas at high frequencies a locally inner oscillating flow structure is observed.
Keywords: Fluid-structure interaction, wall-shear stress, PIV, elastic vessel, stenotic vessel.

Introduction

Cardiovascular diseases cause the majority of deaths in developed countries [1]. Knowledge about the long-term impact of medical surgeries is of utter importance to achieve the best recovery chances, since restenosis still is a problem. Hemodynamic factors play an important role on local vessel proliferation [1, 2] and do also influence the process of restenosis. Numerical simulations, which model the fluid-structure interaction, can provide information about the consequences of different surgery alternatives on the process of restenosis. To be able to model this physical question and to validate these numerical studies, it is necessary to fully understand the fluid-structure interaction between an elastic vessel model and unsteady flow and the interaction between the elasticity of the tissue and the unsteady wall-shear stress.

Experimental investigations of elastic models representing the human aorta using laser-Doppler anemometry revealed the dominant role of the vessel elasticity on the velocity field inside the vessel [3–5]. PIV measurements were used to measure unsteady [6–8] and steady [9] flows in elastic vessels. Nevertheless, non-invasive pressure measurements giving information on the wall normal forces combined with a detection of the time-resolved vessel wall response and the unsteady wall-shear stress distribution are still missing.

In this investigation time-resolved particle-image velocimetry measurements combined with synchronous measurements of the static pressure are applied to a highly elastic, axisymmetric stenosed, transparent vessel model at oscillating, pulsatile flow. The elastic vessel model is manufactured out of Polydimethylsiloxane (PDMS) to mimic the human aorta. The optical, geometric, and structure-mechanical properties of the vessel model are carefully measured. The vessel model is integrated in a refractive index-matched test bench and oscillating flow is generated using a piston pump. The piston pump is driven by a linear actuator generating Reynolds and Womersley number conditions of physiological relevance.

The measurements in the vicinity of and inside the stenosis will reveal details about the influence of the vessel elasticity and geometric change in the stenosis on the velocity field and the static pressure distribution. The response of the elastic vessel wall on the evolving flow field

regarding amplitudes and phase dependences will be investigated using the detected wall position. The TRPIV data yield the unsteady wall-shear stress distribution.

The first part of this paper describes the geometric and mechanical properties of the elastic vessel model together with refractive index matching considerations. The experimental facility and the measurement technique are discussed in the next section. In the second part the data evaluation based on the TRPIV images is introduced. Vessel wall detection, elimination of the wall curvature and wall-shear stress estimation are outlined in detail. The flow field, the wall-shear stress distribution and the static pressure fluctuation as well as the dilatation of the vessel model are investigated in the third part of the paper. The paper concludes with a short discussion and conclusion.

Experimental facility

Elastic vessel model

The fully transparent, elastic vessel model mimics the human aorta in its geometric and structure-mechanical properites. It is made from the two component PDMS RTV 615. The vessel possesses an inner diameter of $D_0 =$ 22 mm in the cylindrical part and a minimum diameter of $D_S = 11$ mm in the stenosis, where the vessel is relatively rigid compared to the non-stenotic parts due to the thicker wall. The vessel length is 450 mm. The length of the stenotic part is 60 mm. To achieve a smooth surface and defined geometry, the vessel model is cast using the core casting method.

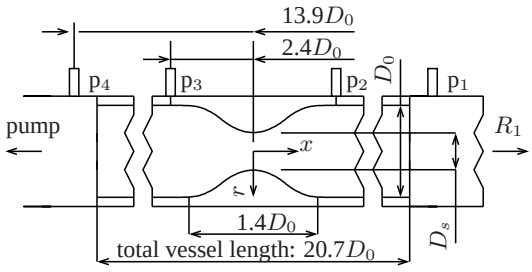

Figure 1 Sketch of stenotic vessel with pressure sensor positions p_1 - p_5

The structure-mechanical properties of the vessel model are determined by measurements of the Young's Modulus and the vessel compliance. The Poisson's number is very close to 0.5 for rubbery polymers (0.499-0.4999999) [10]. For each vessel model a round tensile specimen and a sample to measure the refractive index are cast. The compliance is acquired through measuring the inner-vessel diameter using the PIV measurement setup while pressurizing the vessel model. These measurements are used to calculate the compliance C

$$C = \frac{\partial A/\partial p}{A_0} \approx \frac{2\partial R/\partial p}{R_0},\ [C] = \frac{1}{\text{Pa}} \quad . \tag{1}$$

The quantitiy A represents the vessel cross section, R the inner-vessel radius, and p the static pressure. Initial values are indicated by the index 0. The investigated

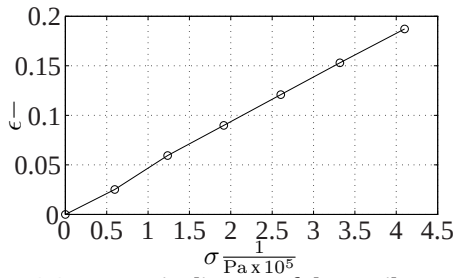

Figure 2 Stress-strain diagram of the tensile specimen

vessel model possesses the compliance $C = 12.31 \cdot 10^{-6}$ $1/\text{Pa}$ and the Young's Modulus $E = 2.17 \cdot 10^6$ Pa (Figure 2). During the mixing process of the RTV 615 components, Rhodamin B solved in 2-Propanol is added to the liquid PDMS components. This gives the material a weak fluorescence which is used to detect the wall. The 2-Propanol volatilizes during the mixing process. To gain optical access without aberrations, a refractive index matching at an accuracy of $\Delta n = 5 \cdot 10^{-3}$ is necessary [11]. By changing the ratio of water and glycerin, the refractive index of the measurement fluid is adapted to that of the PDMS at an accuracy of $\Delta n = 1 \cdot 10^{-3}$. This accuracy is sufficient to detect the near-wall velocity field. To complete the refractive index matching, the vessel model is embedded in a box filled with measurement fluid. The vessel mounting eliminates edge effects changing the behavior of the vessel in the entrance region. Furthermore, it is possible to stretch the PDMS vessel like the human vessel about 10% of its original length in the axial direction. The surrounding fluid has exactly the same properties as the measurement fluid and ensures that buoyant forces are minimized. The experimental facility is built such that it can be assumed to be rigid compared to the elastic vessel such that all effects of elasticity are solely caused by the elastic vessel model. The sinusoidal pulsatile flow at Womersley numbers up to 13 is generated by a piston pump driven by a linear actuator. The initial pressure inside and outside the vessel is regulated via reservoirs (Figure 3).

Measurement technique

Hollow glass spheres with a diameter of 10 μm are used as tracer particles. The entrance length on both sides of the vessel equals $L = 125\, D_0$ with D_0 as the inner vessel diameter. This assures a symmetrical velocity profile at the vessel entrance [12, 13]. The TRPIV setup consists of two

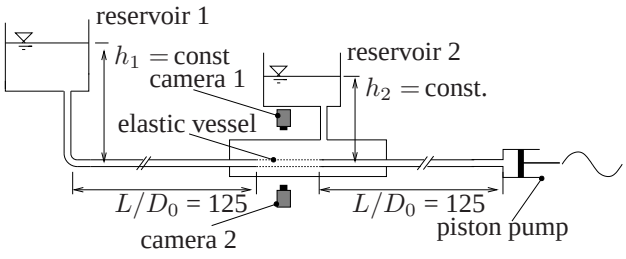

Figure 3 Test bench with entrance length and piston pump

Fastcam PCI 1024 operating at 400 frames per second and a Darwin Duo Nd:YLF laser with a wavelength $\lambda = 527$ nm. The resulting double frame frequency of 200 Hz offers a sufficient temporal resolution to detect unsteady flow phenomena since the maximum frequency in this experiment is 1 Hz. Camera 1 records at a resolution of 34.78 px/mm to determine the velocity distribution in the whole vessel cross section and to detect the inner vessel wall. Camera 2 uses a higher resolution of 55.67 px/mm to measure the wall-shear stress distribution. The light sheet with a thickness of 0.5 mm is aligned to the center axis of the elastic vessel model (Figure 4). The pulse distance is a compromise with respect to the low particle displacement during flow reversal and high particle displacement during cycle peaks. To achieve the best spatial resolution the stenotic part of the vessel is investigated by camera 1 in 6 sections aligned to the center axis of the vessel model (Table 1). Camera 2 records a magnification of the corresponding measurement section.

section	$x_{\min}$	$x_{\max}$
1	-6.36 D_0	-5.45 D_0
2	-2.27 D_0	-0.95 D_0
3	-1.13 D_0	0.04 D_0
4	-0.04 D_0	1.13 D_0
5	0.95 D_0	2.27 D_0
6	5.45 D_0	6.36 D_0

Table 1 Streamwise measurement sections

Two miniature pressure sensors at a diameter of 2.4 mm record the static pressure inside the PDMS vessel at both entrances of the stenosis (Figure 1). The sensor mounting is designed such that the structure-mechanical behavior of the elastic vessel is not changed (Figure 4). Furthermore,

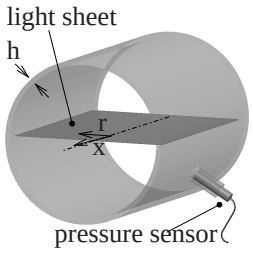

Figure 4 Light sheet alignment and pressure sensor mounting in the elastic vessel model

the pressure at the reservoir facing entrance is measured by one additional pressure sensor. A magnetostrictive path sensor is used to measure the piston movement. The pressure and the piston path measurements are synchronized via the first pulse of the double laser pulse.

Data evaluation

From the TRPIV images the unsteady wall position is detected using the intensity distribution. The fluorescing Rhodamin B emits diffuse light at $\lambda_e = 565$ nm which is independent of the direction of the exciting laser beam. The intensity distribution in the vessel wall region clearly indicates the position of the vessel wall by a steep gradient of the intensity distribution. Inside the silicone material the intensity distribution only shows fluctuations due to measurement noise (Figure 5). This allows to compute the vessel wall position at an accuracy of 2 px. The detected wall position is used to determine the structure response and to align and mask the images to enhance further image processing.

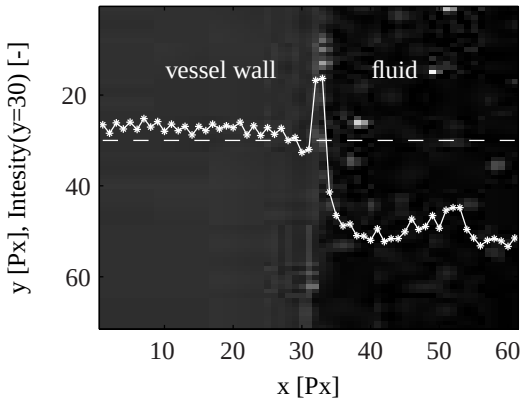

Figure 5 Intensity distribution inside the vessel model

To be able to detect the wall-shear stress distribution from the TRPIV images of camera 2 the curvature of the vessel wall has to be eliminated. A wall transformation algorithm suggested by [14] transforms the curved wall based on the detected vessel wall position into a straight wall. The particle image up to a distance of 50 px from the vessel wall is also transformed (Figure 6 a).

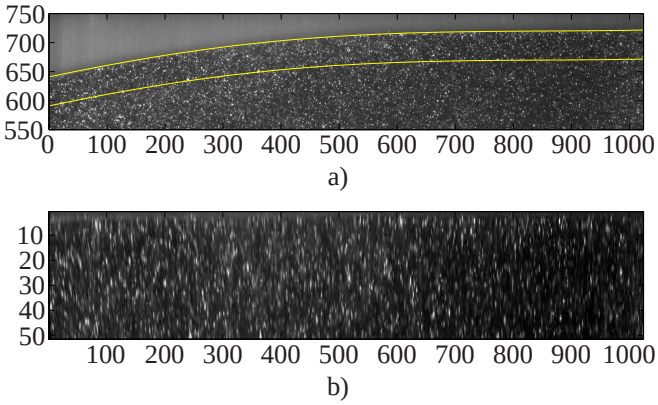

Figure 6 a) PIV image; b) Transformed near-wall PIV image section

The flow field inside the vessel is determined from the PIV images of camera 1 using an FFT-based spatial cross correlation method implemented in the open source code MatPIV. The applied multi-pass algorithm starts using a 64 x 64 px^2 interrogation size with 50% overlap. With an interrogation size of 16 x 16 px^2 and an overlap of 50% in the last step a vector spacing of 0.23 mm is achieved, which corresponds to 0.010 D_0 in the largest cross section

and 0.020 D_S in the stenosis, where $D_S = \frac{D_0}{2}$.

The wall-shear stress distribution is estimated from the transformed particle images from camera 2 (Figure 6 b). In the near-wall region up to a distance of 10 px (0.0081 D_0) from the vessel wall the wall-normal velocity component is assumed to be negligible. Hence, the veloctiy distribution in this region is estimated using an FFT-based cross correlation method with rectangular interrogation spots of the size 32 x 4 px^2 and an overlap of 50%. This results in a resolution of 2 px in the radial direction and 16 px in the axial direction. At the same time it is guaranteed that the interrogation spot contains enough particles to perform the cross correlation. The aquired local velocity profiles are fitted between the 2^{nd} and the 10^{th} pixel from the wall to determine the slope of the velocity profile and thereby the local wall-shear stress. Due to the axis symmetric properties of the flow the wall-shear stress distribution is distributed over the inner circumference of the elastic vessel.

Flow parameters

Using the information in Figure 7 the damped eigenfrequency f_D and the eigenfrequency f_0 of the flow facility can be determined by

$$f_D = f_0 \sqrt{1 - D^2} \quad , \tag{2}$$

$$D = \frac{\delta}{2\,\pi\,f_0} \quad , \tag{3}$$

$$\delta = ln(q)\,f_D \quad , \tag{4}$$

$$q = \frac{y_i}{y_{i+1}} \quad . \tag{5}$$

The damping ratio D can be calculated by the damping coefficient δ, which is determined by the ratio of amplitudes q. The quantities y_i and y_{i+1} represent two successive amplitudes. The damped eigenfrequency in Figure 7 is $f_D = 0.99\,\text{Hz}$ yielding the eigenfrequency to $f_0 = 0.9935\,\text{Hz}$. Since the test facility is considered rigid compared with the elastic vessel, the main properties determining the eigenfrequency are the mass of the measurement fluid and the vessel elasticity. At frequencies near the eigenfrequency the amplitude of the dilatation increases rapidly and reaches its maximum at the eigenfrequency. In experimental facilities with oscillating flow high amplitudes of dilatation lead to a collapsing of the vessel model during backward flow.

In this experiment three cases with different combinations of Reynolds and Womersley numbers are examined. The peak Reynolds number Re_D is calculated by the original vessel diameter D_0 and the maximum bulk velocity $\bar{u}_{max}$ generated by the piston pump. The Womersley number as dimensionless frequency is defined by the kinematic viscosity ν and the angular frequency ω of the piston pump

$$Wo = \frac{D_0}{2}\sqrt{\frac{\omega}{\nu}} \quad . \tag{6}$$

The flow conditions of case 1 are adjusted such that the resulting characteristic parameters are of physiological relevance for large arteries. To investigate higher Womersley numbers in case 2 the Reynolds number had to be reduced significantly to avoid collapsing of the elastic vessel model as the frequency for this Womersley number is near the eigenfrequency. Test case 3 is of interest to provide experimental validation data of flow conditions below and above the eigenfrequency.

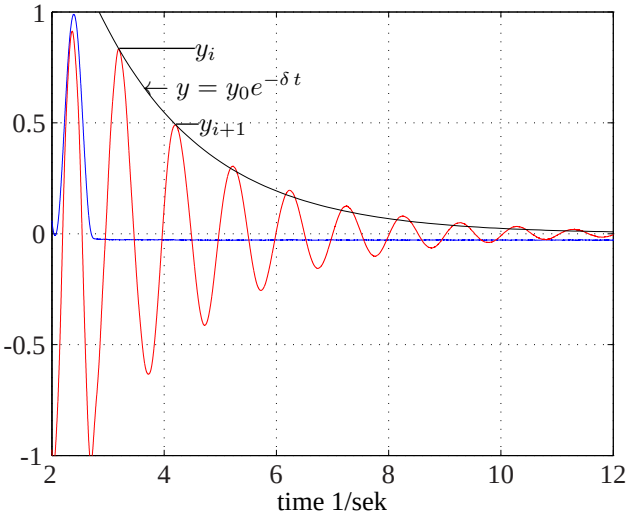

Figure 7 Normalized eigenfrequency oscillation of the static pressure (–) and normalized piston path (–)

These three cases are summarized in Table 2. Additionally, the frequency f and the piston stroke s of the piston pump are given in Table 2. In the following, all given phase angles refer to the phase of the piston (Figure 8).

case	Re_D	Wo	$f\ \frac{1}{\text{Hz}}$	$s\ \frac{1}{\text{mm}}$
1	690	7.5	0.5	8.2
2	310	9.5	0.8	2.28
3	680	13	1.5	2.68

Table 2 Characteristic flow parameters

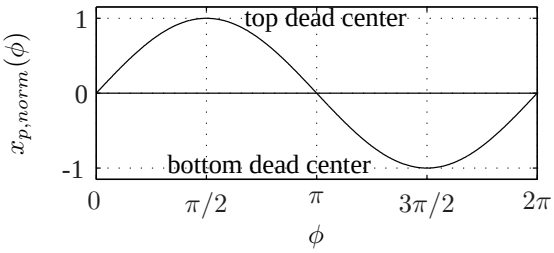

Figure 8 Phase angle definition with normalized piston path $x_{p,norm}(\phi)$

Results

The oscillating flow field

Due to the oscillating flow and the change of the vessel cross section in the stenosis a phase dependent complex flow field develops. Figures 9 - 11 show the unsteady velocity distribution during flow reversal starting at $\phi = \frac{1}{2}\pi$ (top dead center) at 9 phase angles for the three cases 1,

2, and 3. The contours represent the absolute velocity $U = \sqrt{u^2 + v^2}$. Every 10^{th} (case 1), every 6^{th} (case 2), and every 3^{rd} (case 3) time step are displayed. For better visualization only every 8^{th} vector is plotted in these figures.

First case 1 is examined. After flow reversal at $\phi = 0.51\pi$ the velocity in the stenosis increases and a jet at the downstream side of the smallest cross section developes. Due to the divergence of the vessel this jet undergoes an adverse pressure gradient. The flow starts to separate in the downstream part of the stenosis and a ring vortex is generated at $\phi = 0.66\pi$. The ring vortex moves downstream and leaves the center measurement sections at $\phi = 0.81\pi$. Between the downstream moving ring vortex and the separation point a reversed flow region with very low velocities occurs. The jet enters the outer left measurement section at $\phi = 0.91\pi$. This package of disturbed flow can also be seen at $\phi = 0.51\pi$ in the upstream located measurement section. It enters the stenosis at $\phi = 0.61\pi$.

At case 2, flow reversal sets in at $\phi = 0.66\pi$ with a phase lag of $\Delta\phi = 0.1\pi$. The flow patterns are similar to case 1 but at lower peak velocities. Case 3 exhibits a completely different flow pattern. Although the Reynolds number is nearly the same as for case 1, the peak velocities are significantly lower. The velocity distribution in the smallest cross section does not coincide with the bulk flow generated by piston. These observations can be explained with the fact that the pump frequency of case 3 is above the eigenfrequency of the elastic vessel model in the experimental facility. For this frequency range the flow inside the vessel model is not directly related to the flow generated by the piston pump. Therefore, the Reynolds number calculated by the bulk flow does not describe the flow conditions inside the elastic vessel model.

Wall-shear stress

The normalized unsteady wall-shear stress distribution for case 1 - 3 is shown in Figures 12 - 14 as contour plot. The measured wall-shear stress is normalized with the wall-shear stress at steady flow at the same Reynolds number Re_D. The vertical axis displays the streamwise direction of the stenotic vessel. The horizontal axis denotes the phase angle. As phase reference the piston path without its values is plotted at the bottom of the figure. The colormap is adapted for each figure.

The wall-shear stress distributions of case 1 and 2 show a similar pattern. The highest wall-shear stress values occur in the smalles cross section, where the highest velocities can be observed (Figures 9 - 11). The sign-change describes the reversal of the flow direction. Significantly lower values can be observed in both entrances of the stenotic part. The ring vortex, which forms after the flow reversal and then moves downstream, leads to locally inverted flow and sets in an increase of wall-shear stress in the entrance regions. This behaviour can be identified in the wall-shear stress plots of case 1 and 2 as streaks which originate near to the center of the stenosis at the beginning of the high wall-shear stress region and extend to the

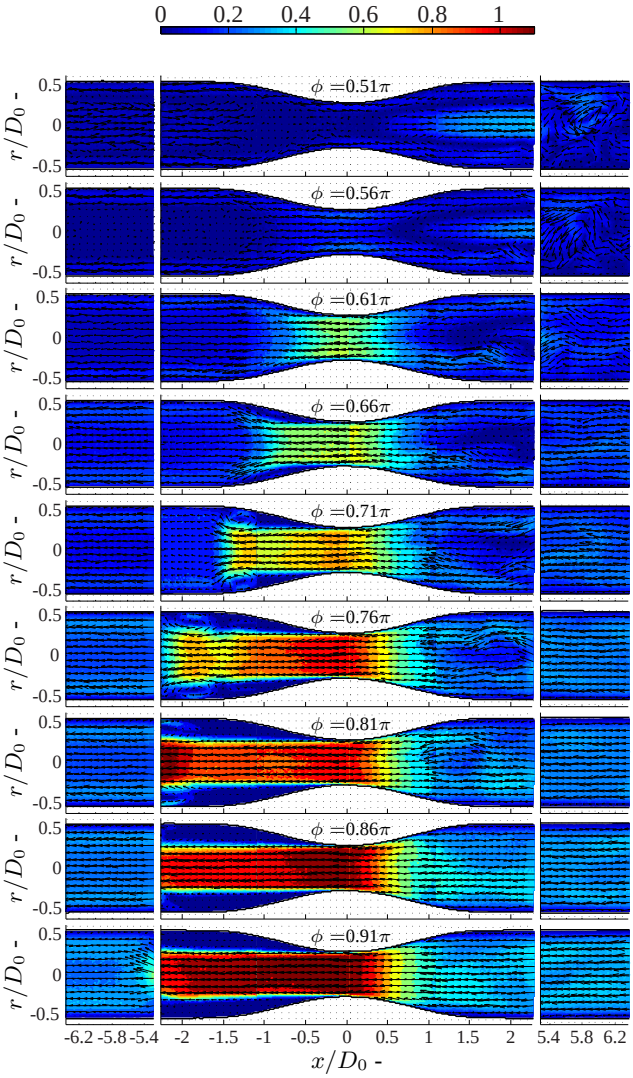

Figure 9 Velocity distribution $U(x,t)$ in $\mathrm{m/s}$ at 9 phase angles for case 1

entrances, where the ring vortex leaves the center measurement sections ($x < -2.2\,D_0$ mm and $x > 2.2\,D_0$ mm).

The wall-shear stress distribution of case 3 shows a totally different pattern compared to case 1 and 2. The frequency of case 3 is above the eigenfrequency of the experimental facility. Case 1 possesses higher wall-shear stress values compared to case 2, which is due to the higher Reynolds number. The wall-shear stress distribution of case 3 possesses the lowest values which correspond to the low velocities (Figure 11).

Static pressure

Figure 15 shows the static pressure measurements for cases 1, 2, and 3 as a function of the phase angle. The static pressure difference Δp_{stat} is defined as follows

$$\Delta p_{stat} = p_{stat}(t) - p_{stat,0} \quad . \tag{7}$$

The quantity $p_{stat,0}$ is the initial static pressure determined by the reservoir and measured prior to every measurement. The green line representing the static pressure difference in

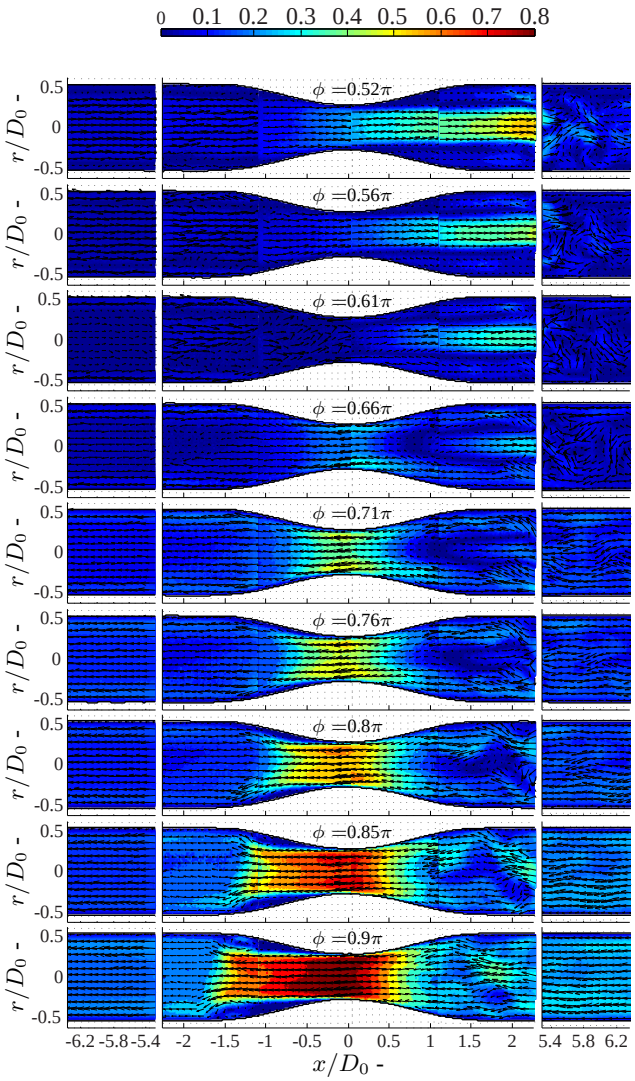

Figure 10 Velocity distribution $U(x,t)$ in $\mathrm{m/s}$ at 9 phase angles for case 2

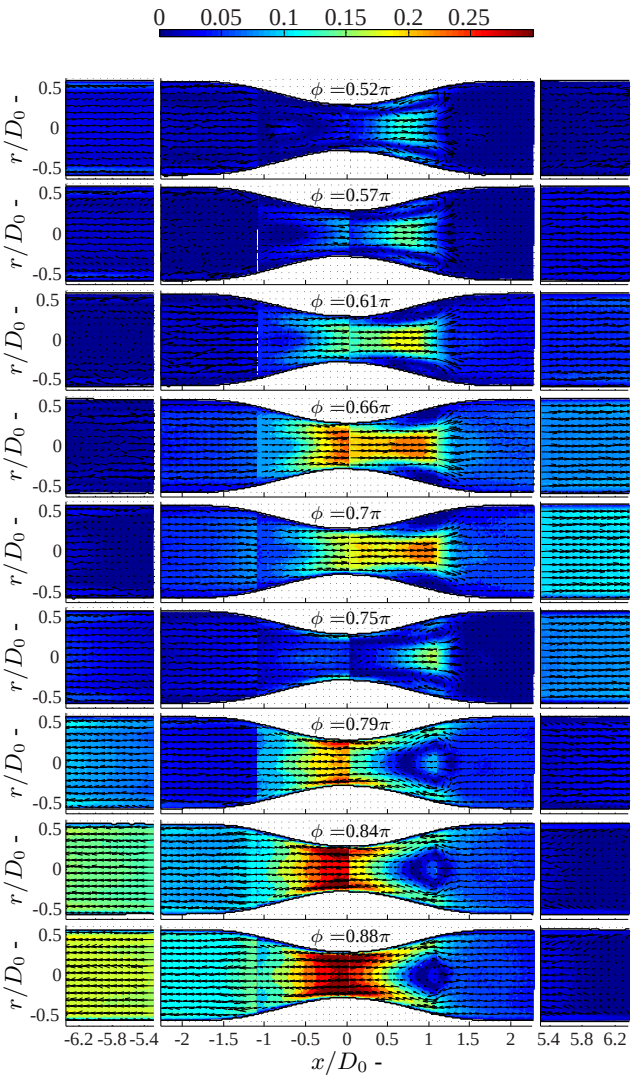

Figure 11 Velocity distribution $U(x,t)$ in $\mathrm{m/s}$ at 9 phase angles for case 3

the stenosis entrance facing the pump possesses the highest amplitude, followed by the blue line marking the static pressure difference in the opposite stenosis entrance, and by the red line denoting the static pressure difference at the elastic vessel entrance facing the reservoir. This result is expected from the theoretical solution of pulsatile pipe flow.

The shape of the pressure curves of case 1 clearly deviates from a sinusoidal curve. The absolute value of the negative peak values is slightly higher compared to the positve peak values. The negative peak value of case 1 coincides with the top dead center of the piston and the phase angle of flow reversal (Figure 9). At case 2 a phase lag of 0.1π between the negative peak of the pressure difference and the top dead center of the piston can be observed. This phase lag was already detected for the phase angle of flow reversal of case 2 (Figure 9). The phase lags of the positive peaks of case 1 and 2 differ from the phase lags of the neagtive peaks. The analysis of the development of the static pressure difference of case 3 shows a very high phase

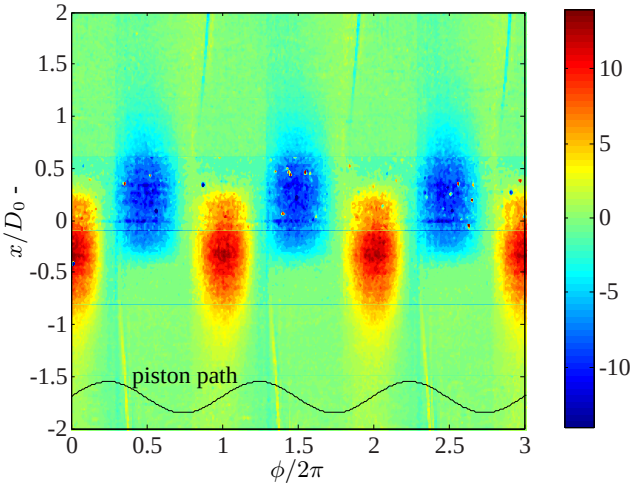

Figure 12 Normalized unsteady wall-shear stress distribution for case 1 and normalized piston path as phase reference

lag of 0.4π of the negative peak to the top dead center of the piston.

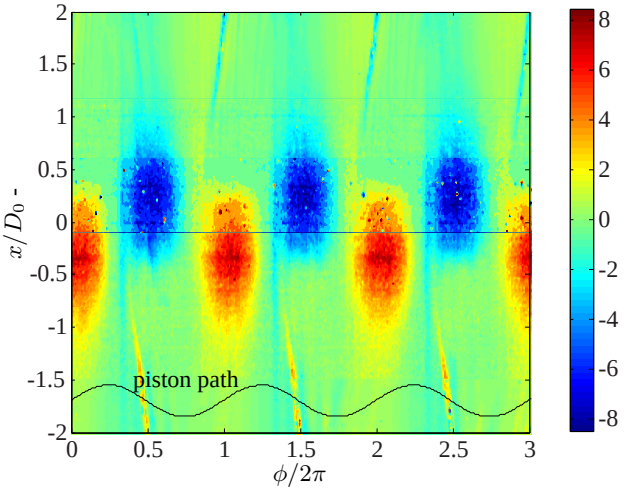

Figure 13 Normalized unsteady wall-shear stress distribution for case 2 and normalized piston path as phase reference

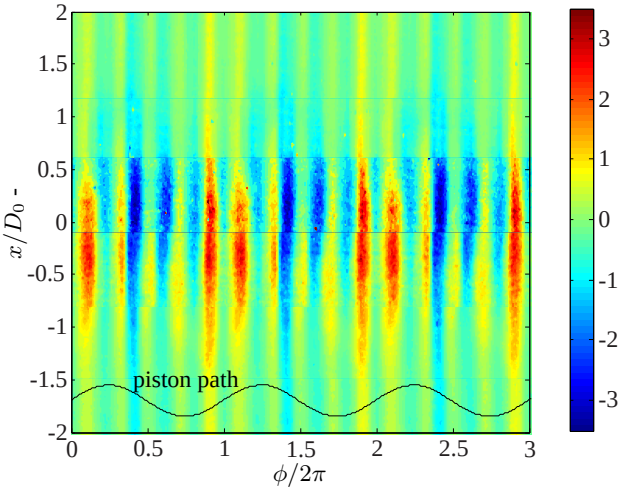

Figure 14 Normalized unsteady wall-shear stress distribution for case 3 and normalized piston path as phase reference

Vessel dilatation

To investigate the coherence of the static pressure difference and the dilatation a comparison of the normalized static pressure difference $p_{stat,norm}$ and the normalized dilatation ϵ_{norm} at several streamwise positions is shown in Figure 16.

$$p_{stat,norm} = \frac{\Delta p_{stat}(t)}{max(\Delta p_{stat}(t))} \quad , \tag{8}$$

$$\epsilon_{norm} = \frac{\epsilon}{max(\epsilon)} \quad , \tag{9}$$

$$\epsilon = \frac{D(t) - D_0}{D_0} \quad . \tag{10}$$

The dilatation is measured at $x = \pm 2\, D_0$ and the static pressure difference at $x = \pm 2.4\, D_0$ (Figure 1). At the reservoir facing side of the stenosis ($x > 0$) $\Delta p_{stat,norm}$ and ϵ_{norm} are aligned for all phase angles of case 1 whereas at case 2 and 3 a small difference in the negative peak values between $\Delta p_{stat,norm}$ and ϵ_{norm} can be observed. At the pump facing side of the stenosis $\Delta p_{stat,norm}$ and ϵ_{norm} are aligned for positive $\Delta p_{stat,norm}$ values but exhibit different negative peak values. No phase lags can be observed in any position of the three cases.

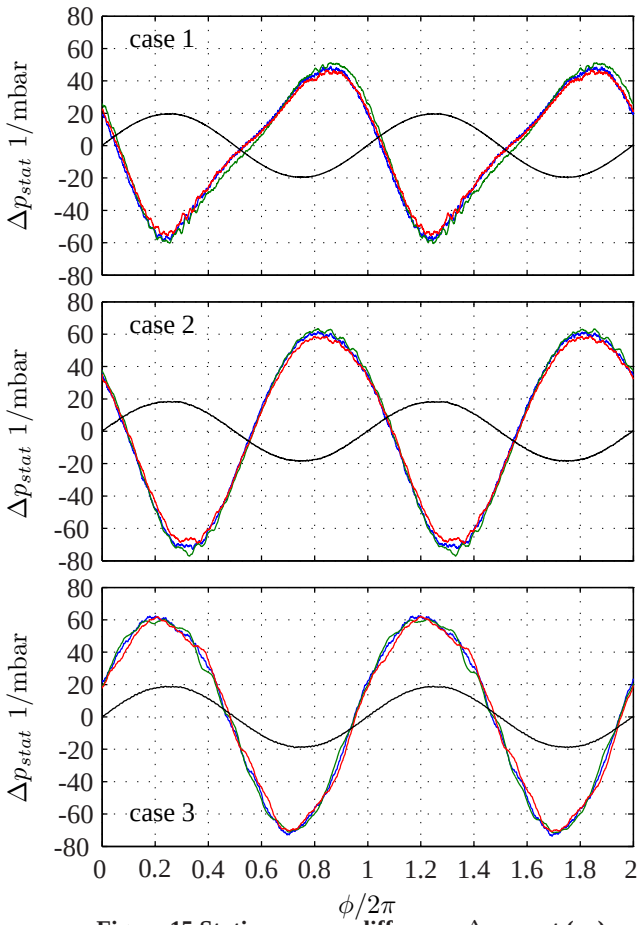

Figure 15 Static pressure difference Δp_{stat} at (—) $x = -1.6\, D_0$, (—) $x = 1.6\, D_0$, and (—) $x = 13.9\, D_0$ for cases 1, 2, and 3 vs. phase angle

The structure-mechanical response of the elastic vessel model on the pulsatile flow is examined using the unsteady vessel dilatation at several streamwise positions. Figure 17 presents the local vessel dilatation ϵ_l

$$\epsilon_l = \frac{D(t,x) - D_0(x)}{D_0(x)} \quad , \tag{11}$$

at the streamwise positions $x = \{\pm 5.4\, D_0;\ \pm 2.2\, D_0;\ \pm 1.3\, D_0\}$ for cases 1, 2, and 3. The quantity $D_0(x)$ represents the initial diameter. The piston path is displayed as black line without its values to clarify phase dependences.

The initial diameters are measured prior to every measurement. The local vessel dilatation strongly depends on the local wall thickness. At $x = \pm 1.3\, D_0$ the local dilatation is only 67% of that at $x = \pm 2.0\, D_0$. The wall thickness at $x = \pm 1.3\, D_0$ is 137.5% of the wall thickness at $x = \pm 2.0\, D_0$. The local dilatation at $x = \pm 1.3\, D_0$ shows the positive peak values to coincide for all cases but the negative peak values to differ at case 1 and case 2. For case 3 high fluctuations can be observed at $x = -5.4\, D_0$ after bottom dead center.

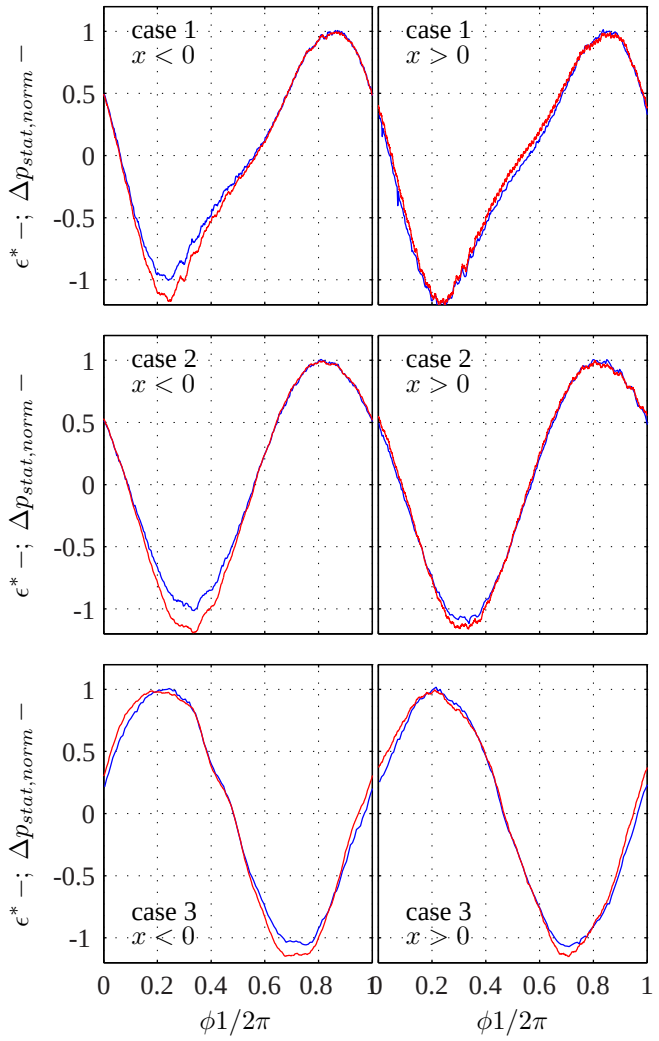

Figure 16 (—) Normalized static pressure difference $\Delta p_{stat,norm}$ at $x = \pm 2.4\, D_0$ and (—) normalized dilatation ϵ_{norm} at $x = \pm 2.0\, D_0$ for cases 1, 2, and 3

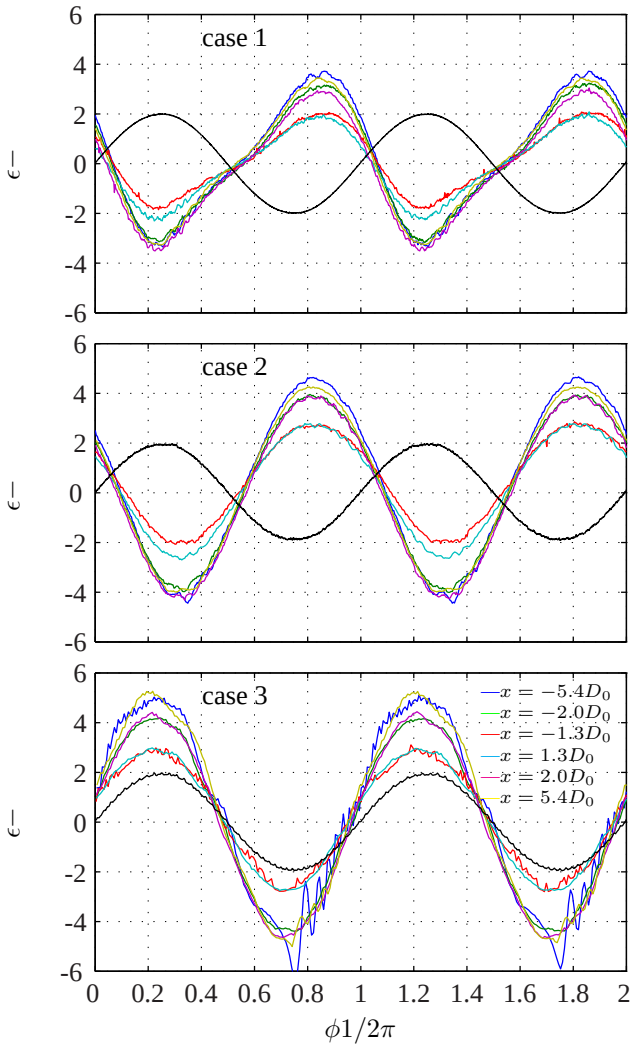

Figure 17 Vessel dilatation ϵ at 6 streamwise positions for case 1 - 3.

Discussion

The unsteady flow field of case 1 and case 2 is dominated by the jet which develops in the smallest cross section due to the decrease of flow area in the stenosis. At the streamwise tip of the jet a ring vortex is generated and transported downstream until flow reversal sets in. The phase angle between the piston motion and the flow response exhibits increasing phase lags for case 1 and 2 compared to the top and bottom dead center of the piston, which are related to the elasticity of the elastic vessel model. The flow pattern of case three significantly deviates from case 1 and 2 since the piston frequency is above the eigenfrequency of the elastic vessel in the experimental facility. That is, a local higher mode oscillation of the mass in the stenotic area occurs.

The unsteady wall-shear stress distribution exhibits increased wall-shear stress in the smallest cross section of the stenosis whereas in the downstream part of the stenosis very low wall-shear stress can be observed. The moving ring vortex temporally increases the wall-shear stress in the downstream part of the stenosis. From a medical point of view, the wall-shear stress distribution along the stenosis during the first ($0 \leq \phi \leq \pi$) or the second half of the flow movement ($\pi \leq \phi \leq 2\pi$) is of utter importance. At pulsatile flow without flow reversal, the ring vortex will probably oscillate around a mean streamwise position and will induce temporally varying higher wall-shear stresses that could have an inflammating effect.

The investigation of the unsteady vessel dilatation and the static pressure difference shows these quantities to perfectly coincide regarding the phase angle. Comparing the change in amplitudes no significant differences between vessel dilatation and static pressure occur. To closer examine the effect of the eigenfrequency on the static pressure difference and the vessel dilatation, a theoretical estimate of the static pressure fluctuation is determined. From the unsteady Bernoulli equation

$$p_{vessel} + \frac{\rho}{2} u^2 = p_0 + \rho\, g\, h_1 + \int_0^{125\, D_0 + h_1} \rho \frac{\partial u}{\partial t} ds \quad , \quad (12)$$

the static pressure inside the vessel model is determined

using the piston generated bulk flow:

$$p_{vessel} = p_0 + \rho \left[g\, h_1 - \frac{1}{2} \left(\frac{1}{2} s \left(\frac{D_k}{D_0} \right)^2 \omega\, cos\phi \right)^2 - \right.$$
$$\left. - \left(125\, D_0 + h_1\right) \frac{1}{2} s \left(\frac{D_k}{D_0} \right)^2 \omega^2\, sin\phi \right] \quad . \qquad (13)$$

The ratio $\left(\frac{D_k}{D_0}\right)^2$ describes the area change from the piston pump into the elastic vessel model. Comparing the order of the amplitudes of the trigonometric expressions in Equation 13

$$\frac{\frac{1}{2}\left(\frac{1}{2} s \left(\frac{D_k}{D_0}\right)^2 \omega\right)^2}{\left(125\, D_0 + h_1\right) \frac{1}{2} s \left(\frac{D_k}{D_0}\right)^2 \omega^2} = \frac{\frac{1}{4} s \left(\frac{D_k}{D_0}\right)^2}{125\, D_0 + h_1} \quad , \qquad (14)$$

results in a ratio of $\frac{7}{1000}$ for the dynamic pressure difference to the unsteady pressure difference. Since the peak values of $(cos\phi)^2$ and $sin\phi$ never coincide, the contribution resulting from the dynamic pressure can be neglected. Hence the theoretical static pressure difference in the elastic vessel model can be expressed by the unsteady pressure term $\rho\,(125 D_0 + h_1) \frac{1}{2} s\, \omega^2\, sin(\phi)$. Table 3 lists the peak values of the normalized theoretical static pressure difference $\Delta p_{stat,th,norm}$, the normalized measured static pressure difference $\Delta p_{stat,norm}$, and the normalized dilatation ϵ_{norm2}. All three, theoretical and measured static pressure difference and dilatation are normalized by the corresponding peak value of case 1. Although this theoretical calculation is just a rough estimate of the static pressure evolution this comparison clearly shows the effect of the frequency response of the elastic system on the flow conditions. This is of specific interest when the fluid-structure interaction is modeled to perform numerical simulations of blood flow in the human body.

case	$\Delta p_{stat,th,norm}$	$\Delta p_{stat,norm}$	ϵ_{norm2}
1	1	1	1
2	0.71	1.2	1.2
3	2.94	1.2	1.2

Table 3 Comparison of normalized theroretical $\Delta p_{stat,theo,norm}$ and measured $\Delta p_{stat,norm}$ static pressure difference peak values and normalized dilatation ϵ_{norm2}

Conclusions

Time-resolved PIV and static pressure measurements have been performed simultaneously in a highly elastic, stenotic vessel model at pulsatile flow at peak Reynolds numbers Re_D from 310 to 690 combined with Womersley numbers from 7.5 to 13. The vessel dilatation of up to 5% of the initial vessel diameter has been detected by the TRPIV images. Using a transformation algorithm to eliminate the curvature of the inner vessel wall the unsteady wall-shear stress distribution has been determined by the TRPIV images.

Using the TRPIV velocity data, the unsteady vessel wall position, and the pressure data the coherence of the static pressure difference and the vessel dilatation has been analyzed. The measured velocity fields exhibit flow separation and ring vortices at the downstream side of the stenosis. The footprints of the ring vortices have been detected in the wall-shear stress distribution as regions of oscillating higher wall-shear stress. The temporal evolution of the static pressure difference has shown phase lags of pressure peaks to be associated with phase lags in the flow reversal. The investigation of local vessel dilatation has evidenced a strong dependence on the local vessel wall thickness. A comparison of the measured static pressure difference with the theoretical static pressure difference calculated by the unsteady Bernoulli equation evidences the frequency response of the elastic system to play an important role in the investigated frequency range. This result emphasises the significance of correctly computing the fluid-structure interaction in numerical simulations of pulsatile flow in elastic vessels.

The presented results clearly demonstrate the capability of the outlined experimental facility and measurement technique to obtain highly accurate data which are required to analyze the phenomenon of fluid-structure interaction and the wall-shear stress distribution in elastic, symmetric stenosed vessels at pulsatile flow.

References

[1] D.N. Ku. Blood flow in arteries. *Annual Review of Fluid Mechanics*, 29:399–434, 1997.

[2] B. Bharadvaj V. Sottiurai R. Mabon S. Glagov C. Zarins, D. Giddens. Caroid bifurcation atherosclerosis. quantitative correlation of plaque localization with flow velocity profiles and wall shear stress. *Circulation Research*, 53(4):502–514, 1983.

[3] B. Mijovic and D. Liepsch. Experimental flow studies in an elastic y-model. *Technology & Health Care*, 11(2):115–141, 2003.

[4] D.D. Duncan, C.B. Bargeron, S.E. Borchardt, O.J. Deters, S.A. Gearhart, F.F. Mark, and M.H. Friedman. The effect of compliance on wall shear in casts of a human aortic bifurcation. *Journal of Biomechanical Engineering*, 112(2):183–188, 1990.

[5] B.D. Kuban and M.H. Friedman. The effect of pulsatile frequency on wall shear in a compliant cast of a human aortic bifurcation. *Journal of Biomechanical Engineering*, 117(2):219–223, 1995.

[6] T. Eguchi, S. Watanabe, H. Takahara, and A. Furukawa. Development of pulsatile flow experiment system and piv measurement in an elastic tube. *Memoirs of the Faculty of Engineering, Kyushu University*, 63:No. 3, 2003.

[7] S.K. Yazdani and J.L. Berry. Development of an in vitro system to assess stent-induced smooth muscle cell proliferation: a feasibility study. *Journal of Vascular and Interventional Radiology*, 20(1):101–106,

Jan 2009.

[8] R. Yamaguchi, H. Ujiie, S. Haida, N. Nakazawa, and T. Hori. Velocity profile and wall shear stress of saccular aneurysms at the anterior communicating artery. *Heart Vessels*, 23(1):60–66, Jan 2008.

[9] N.A. Buchmann and M.C. Jermy. Particle image velocimetry measurements of blood flow in a modeled carotid artery bifurcation. *16th Australian Fluid Mechanics Conference*, 2007.

[10] J. Bicerano. *Prediction of Polymer Properties*. Marcel Dekker, 1993.

[11] S. Burgmann, S. Große, W. Schröder, J. Roggenkamp, S. Jansen, F. Graf, and M. Büsen. A refractive index-matched facility for fluid-structure interaction studies of pulsatile and oscillating flow in elastic vessels of adjustable compliance. *Experiments in Fluids*, 47(4-5), 2009.

[12] F. Durst, S. Ray, B. Ünsal, and O.A. Bayoumi. The development lengths of laminar pipe and channel flows. *Journal of Fluids Engineering Trans ASME*, 127:1154–1160, 2005.

[13] B. Ünsal. *Time-Dependent laminar, transitional and turbulent pipe flows*. PhD thesis, Universität Erlangen-Nürnberg, 2008.

[14] J. J. Jeong and H. J. Sung. PIV measurement of flow around an arbitrarily moving body. *Experiments in Fluids*, 50(4):787–798, 2010.